Laser-driven resonant magnetic soft-x-ray scattering for probing ultrafast antiferromagnetic and structural dynamics

Daniel Schick,[1,†,*] **Martin Borchert,**[1,†] **Julia Braenzel,**[1] **Holger Stiel,**[1] **Johannes Tümmler,**[1] **Daniel E. Bürgler,**[2] **Alexander Firsov,**[3] **Clemens von Korff Schmising,**[1] **Bastian Pfau,**[1] **and Stefan Eisebitt**[1,4]

[1]*Max-Born-Institut für Nichtlineare Optik und Kurzzeitspektroskopie, Max-Born-Straße 2A, 12489 Berlin, Germany*
[2]*Peter Grünberg Institute, Forschungszentrum Jülich GmbH, Wilhelm-Johnen-Straße, 52428 Jülich, Germany*
[3]*Institute for Nanometre Optics and Technology, Helmholtz-Zentrum Berlin, Hahn-Meitner-Platz 1, 14109 Berlin, Germany*
[4]*Institut für Optik und Atomare Physik, Technische Universität Berlin, Straße des 17. Juni 135, 10623 Berlin, Germany*
Corresponding author: schick@mbi-berlin.de

Time-resolved resonant magnetic scattering in the soft-x-ray range is a powerful tool for accessing the spatially resolved and element-specific spin dynamics in magnetic materials. So far, the application of this photon-demanding technique was limited to large-scale facilities. However, upgrades to diffraction-limited storage rings supporting only x-ray pulses beyond 100 ps, and the shift of x-ray free-electron lasers toward attosecond pulses aggravate the competition for beamtime in the picosecond time window, which is of utmost relevance for magnetism research. Here we present the development of a lab-based instrument providing sufficient photon flux up to 1.5 keV photon energy covering the soft-x-ray resonances of transition and rare-earth metal atoms. Our setup features the mandatory tunability in energy and reciprocal space in combination with sub-10 ps temporal resolution, exploiting the broadband emission of a laser-driven plasma x-ray source, which is monochromatized to about 1 eV bandwidth by a reflection zone plate. We benchmark our approach against accelerator-based soft-x-ray sources by simultaneously probing the laser-induced magnetic and structural dynamics from an antiferromagnetically coupled Fe/Cr superlattice. Our development lays the foundation for laser-driven resonant scattering experiments to study ultrafast ordering phenomena of charges, spins, and orbitals.

1. INTRODUCTION

Throughout the last decades, the main focus of the ultrafast magnetism community has been predominantly on ferri- and ferromagnetic (FM) materials [1–3]. Today, the interest in anti-ferromagnetic (AFM) materials is growing because of their unique properties, such as their faster intrinsic time scales [4], their immunity to magnetic (stray) fields, and their advanced application in opto-spintronics [5]. Due to the absence of a net magnetization $M = |\vec{M}_1 + \vec{M}_2| = 0$ in AFM materials with equivalent sublattice magnetizations $\vec{M}_1 = -\vec{M}_2$, conventional pump-probe techniques, such as the time-resolved magneto-optical Kerr or Faraday effect, as well as x-ray magnetic circular dichroism (XMCD), fail to provide a measure of the magnetization, as they depend linearly on the magnetization M. More advanced techniques, such as magnetic second-harmonic generation (SHG) [6], the magnetic Voigt effect [7], or x-ray magnetic linear dichroism (XMLD) [8], can access the AFM order parameter $\mathcal{L} = |\vec{M}_1 - \vec{M}_2|/2$, but they require distinct crystal symmetries and suffer from significant non-magnetic background contributions.

Resonant magnetic soft-x-ray scattering (RMXS) overcomes the limitations of the former methods by combining spectroscopic sensitivity with access to reciprocal space [9]. The relevant resonances at the absorption edges of the transition metal (TM) L edge and rare-earth (RE) M edge enable element selectivity as well as large magnetic contrast. At the same time, the position of the magnetic scattering in reciprocal space is a direct measure of the AFM periodicity in real space, while the integrated magnetic scattering intensity is proportional to $\mathcal{L}^2$. This allows for probing AFM dynamics at its relevant time and length scale in a pump-probe manner utilizing ultrashort soft-x-ray pulses.

Since time-resolved RMXS requires a bright, tunable, and pulsed soft-x-ray source, such experiments have so far been limited to large-scale facilities such as synchrotron-radiation sources [4,10,11] and free-electron lasers (FELs) [12,13]. While FELs are already approaching the attosecond regime [14,15], the ongoing upgrades of most storage rings toward the diffraction limit (DLSR) [16] will increase the default pulse length at most fourth generation synchrotrons above the 100 ps range. This will aggravate the competition at large-scale facilities for experiments with few

picosecond temporal resolution, which are relevant for a plethora of phenomena in ultrafast magnetism, such as all-optical magnetic switching [17], remagnetization processes [18], spin precession dynamics [19,20], laser-driven phase transitions [21,22], as well as spin-lattice-related effects such as ultrafast magnetostriction [23,24], manipulation of the magneto-crystalline anisotropy [25], and heat diffusion in magnetic nanostructures [26], to name only a few.

To that end, a functional and reliable approach to carry out transient RMXS with a few picosecond temporal resolution is mandatory. Although laser-driven high-harmonic generation (HHG) sources [27–29] are steadily increasing in photon flux and now cover the water window up to 500 eV, their brightness in the relevant photon range from 500 to 1300 eV is still too low for RMXS experiments. Therefore, we developed a scattering instrument employing a laser-driven plasma x-ray source (PXS) [30] to generate ultrashort broadband soft-x-ray pulses from below 50 eV to above 1500 eV, covering the magnetically dichroic absorption L and M edges of most TM and RE elements, respectively. To maintain high photon flux, we collect, focus, and monochromatize the soft-x-ray pulses with a few-picosecond duration by a tailored reflection zone-plate (RZP) optic into an in-vacuum diffractometer for time-resolved laboratory RMXS experiments.

In order to demonstrate the performance of the setup and to highlight the power of the RMXS technique, we investigate the photo-induced dynamics in an AFM-coupled Fe/Cr superlattice (SL) [31]. These artificial magnets typically provide sample structures of high structural quality with tailored functionality, leading to a high technological relevance, e.g., due to the giant magneto-resistance (GMR) effect [32,33]. By spectroscopically recording the reflectivity of the superlattice around the dichroic Fe L_3 resonance, we demonstrate the energy tunability and characterize the energy resolution of our instrument. We show static reciprocal space scans, which clearly evidence the resonant magnetic scattering off an AFM Bragg peak, which was, so far, inaccessible for lab-based instruments. In addition to the magnetic scattering, the large artificial unit cell of the Fe/Cr SL also leads to structural Bragg peaks, which we here exploit to provide access to the lattice dynamics [34] in one and the same experiment. By simultaneously probing the amplitude of the AFM Bragg peak and the shift of the structural Bragg peak after excitation, we are able to directly relate structural and magnetization dynamics, providing an ultimate understanding of the underlying coupling mechanisms of these two degrees of freedom on ultrafast time scales. Our instrumental

approach enables a broad class of time-resolved experiments on ordering phenomena so far only feasible at large-scale facilities. In particular, it allows us to investigate the coupling of different degrees of freedom, such as spins and the lattice, on the relevant picosecond time and nanometer length scale.

2. MATERIALS AND METHODS

We produce pulses of monochromatized soft x-rays and tune them across the Fe L-absorption edges. The photons are scattered off the sample into a detector within a diffractometer setup as shown in Fig. 1. The driver for the PXS is an in-house-developed double-stage thin-disk amplified laser, producing pulses with a duration of 2 ps full width at half-maximum (FWHM) at a wavelength of 1030 nm with a sizable pulse energy of 150 mJ at 100 Hz repetition rate [35]. A pump beam for sample excitation is extracted from the same laser via a 3:97 beam splitter, where the larger part is focused into the vacuum chamber hosting the PXS. At the laser focus of ≈ 15 μm diameter FWHM, a spinning tungsten cylinder is placed under an angle of $45°$. Upon laser excitation of the tungsten target, a plasma is generated, which emits broadband x-ray radiation [30] in the range of 50–1500 eV into the full solid angle. The x-ray photon flux at the relevant Fe L edges (695–735 eV) has been determined to be 5.6×10^{11} ph s^{-1}eV^{-1}sr^{-1} by a calibrated spectrometer at the source. The full spectrum is shown as an inset in Fig. 1. The intrinsic time scales of the x-ray generation processes involved depend on the pulse duration of the driver laser and the lifetime of the electrons inside the plasma. Our results on probing sub-picosecond (ps) dynamics in the Fe/Cr superlattice allow for determining the actual x-ray pulse duration to be below 10 ps; see Section 3.

We chose an RZP [36] as the *single* optical element to collect, disperse, and focus the x-rays from the point-like PXS with a diameter of ≈ 40 μm FWHM toward the sample position. The RZP is placed 1000 mm away from the source point at a grazing incidence angle of $2.0°$, operating at an exit angle of $3.6°$. The calculated magnification of the RZP is 7.2 at its focus position 4000 mm downstream. The distances between source, RZP, and focus represent a compromise between obtaining a large collection angle and a sufficient resolving power of $E/\Delta E = 200$ with a focus of approximately 288 μm FWHM. We estimate the detectable photon flux at the sample position as 1.2×10^6 ph s^{-1}eV^{-1}, which compares well with laser slicing facilities [37] or hard-x-ray PXS sources [38,39].
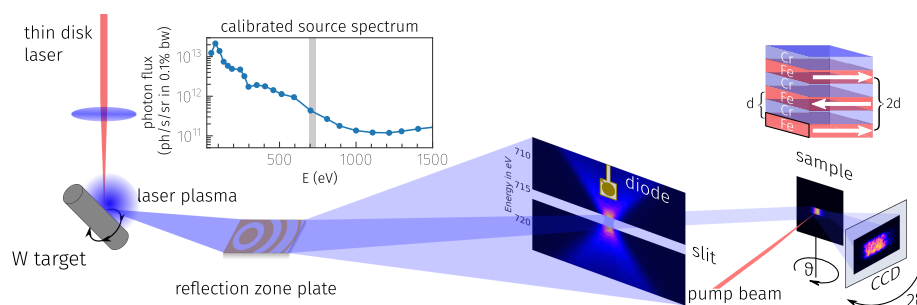
Fig. 1. High-energy laser pulses are focused onto a rotating and translating tungsten cylinder, emitting broadband soft-x-ray radiation into the full solid angle via laser-plasma generation. The inset shows the emitted spectral distribution as measured by a calibrated spectrometer at the source, and the gray area indicates the energy range around the Fe L_3 and L_2 edges from 695 to 735 eV. A reflection zone plate captures this part of the x-rays that are simultaneously focused and dispersed onto an adjustable slit for monochromatization. Part of the blocked x-rays are detected by an x-ray-sensitive SiC diode for normalization. Monochromatic soft x-rays pass the slit and resonantly scatter off the antiferromagnetic Fe/Cr superlattice, as depicted in the upper right scheme, in a ϑ–2ϑ-geometry onto a CCD. The pump beam is used to excite the sample at variable delays.

We increase the nominal energy resolution of the beamline to about 1.2 eV by closing a variable slit down to 100 µm at the focus position of the RZP. In order to scan the photon energy across the 40 eV range, including the Fe L_3 and L_2 absorption edges, we tilt the RZP pitch by only a few millidegrees [37]. For photon energies far away from the RZP's design energy of 705 eV, this procedure results in a decrease in energy resolution and an increase of the horizontal focus size as depicted by the RZP focus image at the slit position in Fig. 1. The latter issue can be addressed by horizontal slits in order to fix the x-ray spot size on the sample. Access to resonances of other magnetic elements is readily provided by additional RZPs mounted on the same manipulator [37].

The sample and a CCD detector are mounted onto an in-vacuum $\vartheta - 2\vartheta$ diffractometer setup at room temperature. The previously split-off pump beam can be delayed by a mechanical stage and is coupled into the vacuum while being focused onto the sample. We use a pump focus diameter of approx. 500 µm FWHM with an incident fluence of 66 mJ/cm². The actual absorbed fluence in the sample can be estimated as only 7%–18% of the incident fluence due to reflectivity of the pump light at the sample surface and spot size broadening for the relevant range of incidence angles ϑ. In order to account for the intensity fluctuations of the PXS due to the mechanical instabilities and material inhomogeneities of the rotating target, we use an IR-insensitive SiC photodiode, mounted onto the slit blades, monitoring part of the blocked x-ray intensity.

The Fe/Cr SL sample was grown on a GaAs substrate by molecular beam epitaxy (MBE). Twenty repetitions of 0.9 nm thick Fe and 0.9 nm thick Cr layers were grown onto a 150 nm thick Ag buffer layer and capped by a single 0.9 nm thick Fe layer and a 2 nm thick MgO layer for oxidation protection. The individual Fe layers are aligned ferromagnetically in-plane as in standard thin-film samples, but the individual layers couple antiferromagnetically along the out-of-plane direction as seen in the sample sketch in Fig. 1 (top right).

3. RESULTS AND DISCUSSION

The artificial periodicity of the repeated Fe/Cr double-layer thickness $D_{DL} = 1.8$ nm enables us to access structural Bragg peaks even with soft x-rays of a few-nanometer wavelength [34]. We define the position of the first-order structural Bragg peak (SL1) as $L = 1$ in reciprocal lattice units (rlu). In addition to the structural periodicity, the AFM order causes a super-periodicity of two Fe/Cr double layers, containing two antiparallel aligned FM Fe layers [40]. Hence, the AFM order leads to purely magnetic half-order Bragg peaks at $L = n/2$ ($n \in \mathbb{N}$). For the special case of the symmetric 0.9 nm Fe and 0.9 nm Cr double layers, only odd diffraction orders are allowed, and no magnetic scattering contributes to the structural Bragg peaks.

In order to probe the AFM Bragg peak, tuning of the photon energy to the magnetically relevant resonances is vital. We first determine the reflection spectrum of the Fe/Cr SL around the Fe L_3 and L_2 absorption edges. To that end, the sample and detector are aligned at $\vartheta = 10°$ ($2\vartheta = 20°$) to benefit from a high sample reflectivity and a rather small L-dependence of the reflectivity far away from the magnetic and structural Bragg peaks. By scanning the incident photon energy, we fully resolve the Fe L_3 and L_2 absorption edges as shown in Fig. 2. We use a linear conversion of the RZP pitch angle to the photon energy transmitted by the RZP monochromator by comparing the experimental data to a
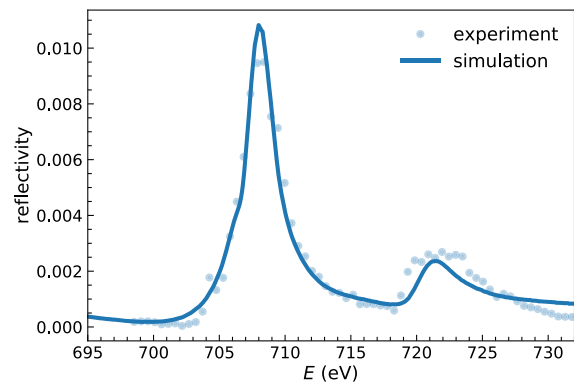
Fig. 2. Reflectivity spectrum around the Fe L_3 and L_2 absorption edges of the Fe/Cr SL, measured at a grazing incidence angle $\vartheta = 10°$. The solid line represents a simulation including magnetic and charge scattering. The experimental data was scaled in intensity to fit the simulation.

simulated spectrum [41]. The calculation relies on high-resolution atomic and magnetic form factors from synchrotron measurements and incorporates variations of the layer thickness, density, and Gaussian roughness [42].

The experimental and simulated reflection spectra agree well and justify the working principle of the RZP-based monochromator. Moreover, we can determine the resolution of the spectrometer by convoluting the simulated spectrum with a Gaussian of variable width and fit it to the experimental data. This fit yields a resolution of 1.5 ± 0.2 eV FWHM at the Fe L_3 absorption edge and is slightly larger than the estimated resolution of 1.2 eV for a 100 µm slit size. The broadening of the Fe L_2 peak in the experimental data can be explained by the decrease of spectral resolution of the RZP further away from its design energy of 705 eV. In order to achieve a simulation-independent energy calibration of the setup, a thin Fe foil can be placed in the polychromatic x-ray beam upstream of the RZP. This will lead to distinct absorption lines in the focus of the RZP, which can be used for calibration [43].

For the following experiments, we fix the x-ray photon energy to the maximum of the Fe L_3 absorption edge around 707 eV. We perform a static $\vartheta - 2\vartheta$ scan, also known as L-scan, and indeed detect the structural SL1 Bragg peak as well as the AFM SL0.5 superstructure diffraction peaks; see Fig. 3. To validate the resonant magnetic nature of the SL0.5 peak, we compare it to an off-resonant L-scan at $E = 680$ eV, which shows the presence of the structural Bragg peak with the AFM Bragg peak being absent due to the lack of magnetic contrast.

This data at the Fe L_3 edge undoubtedly proves resonant magnetic scattering from a laser-driven soft-x-ray source. In addition, we compare the on-resonant experimental data, (scaled in intensity) with a magnetic scattering simulation of the same sample structure [41] and again find a good agreement. This corroborates the use of our normalization scheme, covering more than two orders of scattering intensity variation. However, for reflectivities below 10^{-4}, a feasible signal-to-noise ratio of our current setup is reached. We want to highlight that although the magnetic scattering cross section depends on the x-ray polarization and magnetization direction of the sample [44], resonant magnetic scattering is still feasible with the unpolarized and temporally incoherent PXS.

After determining the optimum x-ray photon energy and positions in reciprocal space, we probe the dynamics of the AFM
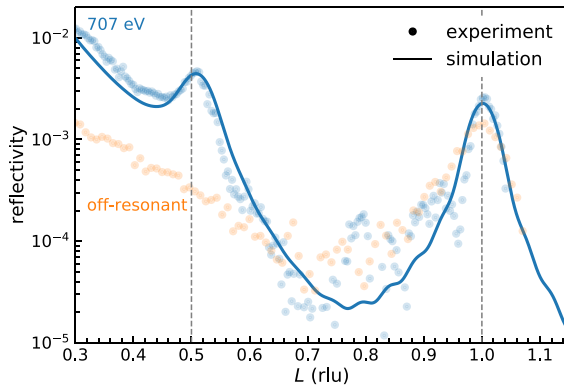
Fig. 3. Static L-scan of the Fe/Cr SL at resonance ($E = 707$ eV, blue dots) and off resonance ($E = 680$ eV, orange dots). The blue solid line represents a scattering simulation of the sample structure including magnetic and charge scattering. At $L = 1$ the structural Bragg peak is present for both photon energies, while the AFM Bragg peak at $L = 0.5$ only appears on-resonance and is also reproduced by the simulations. The experimental data was scaled in intensity to fit the simulation.
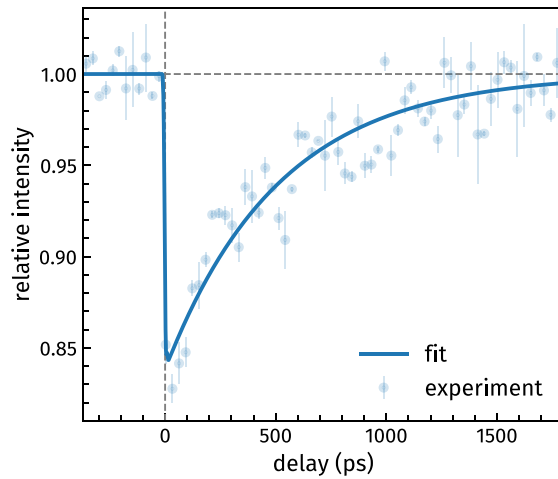
Fig. 4. Average of multiple delay scans of the SL0.5 AFM Bragg peak intensity at the Fe L_3 absorption edge. The peak intensity decreases within a few ps and recovers over hundreds of ps upon photoexcitation, tracing the magnetic response of the sample. The solid line represents a double-exponential fit, and the error bars indicate a confidence interval of 67%.

order and lattice after photoexcitation. The temporal overlap of the pump pulses and the residual IR pulses in the probe beam is determined by sum-frequency generation in a beta-barium borate (BBO) crystal at the sample position. For probing the AFM order parameter, we record the scattered intensity of the AFM Bragg peak at $L = 0.5$ at the L_3 absorption edge as a function of pump-probe delay as shown in Fig. 4.

The delay scan shows a sharp drop of the magnetic SL0.5 peak intensity upon excitation at delay $t = 0$ ps within a few ps and a slow recovery over more than a nanosecond. These dynamics can be well explained by an ultrafast quenching of FM order in the individual Fe layers due to the excitation of electrons by the intense pump pulses and a subsequent loss of AFM order within the whole SL. The underlying processes of the demagnetization can include sub-ps effects such as direct field-driven transfer of spins [45,46], super-diffusive spin transport [2], and Elliot–Yafet-like spin-flip
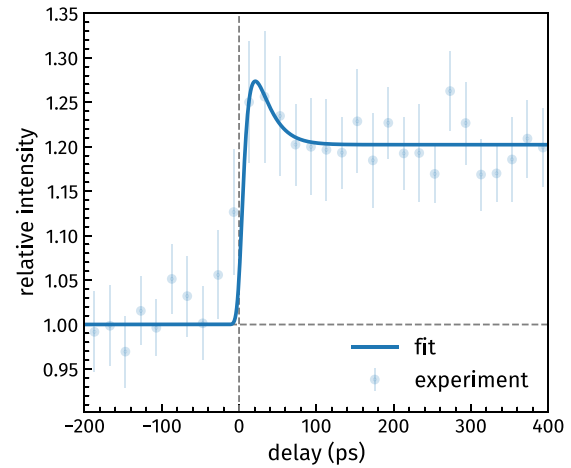
Fig. 5. Average of multiple delay scans on the low-angle side of structural SL1.0 peak at $L = 0.95$. The rapid rise of the signal is due to a Bragg peak shift toward smaller L because of the photoinduced lattice expansion. The double-exponential fit is a guide to the eye and does not fully account for the complex phonon dynamics and the corresponding translation of peak shift and broadening into an intensity variation. The error bars indicate a confidence interval of 67%.

scattering [47]. As the demagnetization is at least an order of magnitude faster than the expected soft-x-ray pulse duration, we use the rapid signal drop to determine the upper bound of the temporal resolution of the RMXS experiment. We extract the temporal resolution from a fit with a double-exponential decay-recovery function convoluted by a Gaussian $g(t)$ with variable width σ to the raw data of Fig. 4 as shown by the solid line.

$$\mathcal{L}^2(t) = e^{-t^2/2\sigma^2} \circledast \left(A e^{-t/\tau_1} + B e^{-t/\tau_2} \right).$$

The decay constant τ_1 is fixed to the 2 ps duration of the pump pulses, as the magnetization is guaranteed to be quenched within this time frame. The fit parameter σ represents the temporal resolution, which is predominately governed by the duration of the x-ray pulses, which we find to be $\sigma = 9 \pm 3$ ps FWHM as an upper bound. The recovery of the AFM order takes up to 1.5 ns, again following an exponential dependency. The de- and remagnetization amplitudes have been determined as $A = -B = 0.16$.

The photoexcited electrons also couple to the lattice degree of freedom by launching coherent and incoherent phonons. The temporal resolution of the PXS is ideally suited to follow the few-ps expansion of the Fe/Cr SL due to the excitation of coherent acoustic phonons (sound waves) [34,48], typically resulting in a pronounced shift of the structural Bragg peak. To demonstrate this capability, we plot the scattered intensity at the low-angle slope of the structural SL1 Bragg peak at $L = 0.95$, as seen in Fig. 5, to translate the peak shift into an intensity modulation of the detected x-ray signal.

The experimental data show a rise of the signal around delay $t = 0$ ps estimated to be within about 20 ps as the lattice expansion shifts the SL1 Bragg peak to lower L and leads to significant peak broadening. The delay time for the maximum expansion of the SL after photoexcitation is determined by the time it takes coherent acoustic phonons to travel once across the SL with a thickness $D_{SL} \approx 37$ nm. Assuming bulk longitudinal acoustic sound velocities, $v_{Fe} = 4910$ m/s and $v_{Cr} = 5940$ m/s, results in a travel time of approximately 7.5 ps, which matches well with the observed rise time of the measured intensity. The recovery of the Bragg peak

position happens again on a ns time scale (not shown) and provides important information about heat diffusion within the SL with its high density of interfaces.

The two delay scans of the AFM SL0.5 and structural SL1 Bragg peaks provide direct access to the relevant time scales of the underlying spin and lattice dynamics. In the future, the full potential of transient RMXS will be exploited by time-resolved L-scans around both Bragg peaks, paving the way to a full spatiotemporal map of the correlated spin and lattice dynamics further complemented by comparison to simulations [41,48,49]. Such experiments will eventually provide access to layer systems containing non-collinear and incommensurate AFM spin structures as well as cases where non-equilibrium spin structures can appear transiently, e.g., during de- and remagnetization processes.

4. CONCLUSION

We present the first resonant magnetic scattering results from a soft-x-ray scattering instrument that we have developed to realize time-resolved lab-based experiments with ps time resolution, in particular, on magnetic samples. In our instrument, an RZP monochromatizes and focuses the broadband emission from a laser-driven plasma x-ray source. Tuning the photon energy to the Fe L_3 resonance, we achieve a photon flux of 1.2×10^6 ph s^{-1}eV^{-1} at the sample position, which, so far, had remained unavailable in the laboratory context. We determine the pulse duration of the x-ray source to be 9 ± 3 ps, which allows for accessing the rich physics of spin–lattice interactions on a ps time scale, as well as magnon, phase-transition, and remagnetization/nucleation dynamics up to several ns delay. We demonstrate the performance of our setup by presenting a full set of static and transient resonant scattering data on an AFM-coupled Fe/Cr superlattice. Our instrument is able to fully resolve the Fe L_3 and L_2 absorption edges in a reflection spectrum. A resonant reciprocal-space scan proves the existence of a half-order Bragg peak due to the AFM coupling of consecutive layers. Realizing the simultaneous detection of the dynamics of the superlattice structure and the interlayer magnetic order in a time-resolved experiment, we achieve the first important milestone to comprehensively investigate correlated spin–lattice dynamics. The setup can be further improved by nonlinear optical up- or downconversion of the pump light, e.g., by pumping an additional optical parametric chirped pulse amplification (OPCPA) stage with part of the thin disk laser output [50]. This eventually enables the generation of photons in the mid-infrared range to resonantly excite phonon modes and to directly control magnetic order via spin–lattice interactions [51,52]. Our laboratory-based approach will further allow us to particularly study the influence of external parameters such as magnetic fields and temperature in great detail. Such experiments will significantly contribute to the field of picosecond dynamics in condensed matter, such as for charge, spin, and orbital ordering in correlated materials. We are convinced that our laboratory-based approach is not only an alternative but eventually a replacement for ps scattering experiments at synchrotron facilities, many of which will soon undergo a DLSR upgrade, making sub-100 ps pulses at these facilities hardly available.

†These authors contributed equally to this paper.

REFERENCES

1. E. Beaurepaire, J.-C. Merle, A. Daunois, and J.-Y. Bigot, "Ultrafast spin dynamics in ferromagnetic nickel," Phys. Rev. Lett. **76**, 4250–4253 (1996).
2. M. Battiato, K. Carva, and P. M. Oppeneer, "Superdiffusive spin transport as a mechanism of ultrafast demagnetization," Phys. Rev. Lett. **105**, 027203 (2010).
3. I. Radu, K. Vahaplar, C. Stamm, T. Kachel, N. Pontius, H. A. Dürr, T. A. Ostler, J. Barker, R. F. L. Evans, R. W. Chantrell, A. Tsukamoto, A. Itoh, A. Kirilyuk, T. Rasing, and A. V. Kimel, "Transient ferromagnetic-like state mediating ultrafast reversal of antiferromagnetically coupled spins," Nature **472**, 205–208 (2011).
4. N. Thielemann-Kühn, D. Schick, N. Pontius, C. Trabant, R. Mitzner, K. Holldack, H. Zabel, A. Föhlisch, and C. Schüler-Langeheine, "Ultrafast and energy-efficient quenching of spin order: antiferromagnetism beats ferromagnetism," Phys. Rev. Lett. **119**, 197202 (2017).
5. P. Němec, M. Fiebig, T. Kampfrath, and A. V. Kimel, "Antiferromagnetic opto-spintronics," Nature Physics **14**, 229–241 (2018).
6. M. Fiebig, V. V. Pavlov, and R. V. Pisarev, "Second-harmonic generation as a tool for studying electronic and magnetic structures of crystals: review," J. Opt. Soc. Am. B **22**, 96 (2005).
7. V. Saidl, P. Němec, P. Wadley, V. Hills, R. P. Campion, V. Novák, K. W. Edmonds, F. Maccherozzi, S. S. Dhesi, B. L. Gallagher, F. Trojánek, J. Kuneš, J. Železný, P. Malý, and T. Jungwirth, "Optical determination of the Néel vector in a CuMnAs thin-film antiferromagnet," Nat. Photonics **11**, 91–96 (2017).
8. T. Moriyama, K. Oda, T. Ohkochi, M. Kimata, and T. Ono, "Spin torque control of antiferromagnetic moments in NiO," Sci. Rep. **8**, 14167 (2018).
9. S. B. Wilkins, P. D. Hatton, M. D. Roper, D. Prabhakaran, and A. T. Boothroyd, "Soft x-ray resonant magnetic diffraction," Phys. Rev. Lett. **90**, 187201 (2003).
10. H. Ehrke, R. I. Tobey, S. Wall, S. A. Cavill, M. Först, V. Khanna, T. Garl, N. Stojanovic, D. Prabhakaran, A. T. Boothroyd, M. Gensch, A. Mirone, P. Reutler, A. Revcolevschi, S. S. Dhesi, and A. Cavalleri, "Photoinduced melting of antiferromagnetic order in La$_{0.5}$Sr$_{1.5}$MnO$_4$ measured using ultrafast resonant soft x-ray diffraction," Phys. Rev. Lett. **106**, 25–28 (2011).
11. K. Holldack, N. Pontius, E. Schierle, T. Kachel, V. Soltwisch, R. Mitzner, T. Quast, G. Springholz, and E. Weschke, "Ultrafast dynamics of antiferromagnetic order studied by femtosecond resonant soft x-ray diffraction," Appl. Phys. Lett. **97**, 062502 (2010).
12. T. Kubacka, J. A. Johnson, and M. C. Hoffmann, et al., "Large-amplitude spin dynamics driven by a THz pulse in resonance with an electromagnon," Science **343**, 1333–1336 (2014).
13. M. Först, A. D. Caviglia, and R. Scherwitzl, et al., "Spatially resolved ultrafast magnetic dynamics initiated at a complex oxide heterointerface," Nat. Mater. **14**, 883–888 (2015).
14. N. Hartmann, G. Hartmann, and R. Heider, et al., "Attosecond time-energy structure of x-ray free-electron laser pulses," Nat. Photonics **12**, 215–220 (2018).
15. S. Serkez, G. Geloni, S. Tomin, G. Feng, E. V. Gryzlova, A. N. Grum-Grzhimailo, and M. Meyer, "Overview of options for generating high-brightness attosecond x-ray pulses at free-electron lasers and applications at the European XFEL," J. Opt. **20**, 024005 (2018).
16. M. Yabashi and H. Tanaka, "The next ten years of x-ray science," Nat. Photonics **11**, 12–14 (2017).
17. L. Le Guyader, M. Savoini, S. El Moussaoui, M. Buzzi, A. Tsukamoto, A. Itoh, A. Kirilyuk, T. Rasing, A. V. Kimel, and F. Nolting, "Nanoscale

sub-100 picosecond all-optical magnetization switching in GdFeCo microstructures," Nat. Commun. **6**, 5839 (2015).

18. L. Willig, A. von Reppert, M. Deb, F. Ganss, O. Hellwig, and M. Bargheer, "Finite-size effects in ultrafast remagnetization dynamics of FePt," Phys. Rev. B **100**, 224408 (2019).

19. R. R. Subkhangulov, A. B. Henriques, P. H. O. Rappl, E. Abramof, T. Rasing, and A. V. Kimel, "All-optical manipulation and probing of the d–f exchange interaction in EuTe," Sci. Rep. **4**, 4368 (2014).

20. T. Gerrits, H. A. M. van den Berg, J. Hohlfeld, L. Bär, and T. Rasing, "Ultrafast precessional magnetization reversal by picosecond magnetic field pulse shaping," Nature **418**, 509–512 (2002).

21. G. Ju, J. Hohlfeld, B. Bergman, R. J. Van Deveerdonk, O. N. Mryasov, J. Y. Kim, X. Wu, D. Weller, and B. Koopmans, "Ultrafast generation of ferromagnetic order via a laser-induced phase transformation in FeRh thin films," Phys. Rev. Lett. **93**, 197403 (2004).

22. F. Büttner, B. Pfau, and M. Böttcher, et al., "Observation of fluctuation-mediated picosecond nucleation of a topological phase," Nat. Mater. **20**, 30–37 (2021).

23. A. von Reppert, J. Pudell, A. Koc, M. Reinhardt, W. Leitenberger, K. Dumesnil, F. Zamponi, and M. Bargheer, "Persistent nonequilibrium dynamics of the thermal energies in the spin and phonon systems of an antiferromagnet," Struct. Dyn. **3**, 054302 (2016).

24. A. H. Reid, X. Shen, and P. Maldonado, et al., "Beyond a phenomenological description of magnetostriction," Nat. Commun. **9**, 388 (2018).

25. J. W. Kim, M. Vomir, and J. Y. Bigot, "Controlling the spins angular momentum in ferromagnets with sequences of picosecond acoustic pulses," Sci. Rep. **5**, 8511 (2014).

26. J. Pudell, A. A. Maznev, M. Herzog, M. Kronseder, C. H. Back, G. Malinowski, A. von Reppert, and M. Bargheer, "Layer specific observation of slow thermal equilibration in ultrathin metallic nanostructures by femtosecond x-ray diffraction," Nat. Commun. **9**, 3335 (2018).

27. S. M. Teichmann, F. Silva, S. L. Cousin, M. Hemmer, and J. Biegert, "0.5-keV soft x-ray attosecond continua," Nat. Commun. **7**, 11493 (2016).

28. C. Kleine, M. Ekimova, G. Goldsztejn, S. Raabe, C. Strüber, J. Ludwig, S. Yarlagadda, S. Eisebitt, M. J. J. Vrakking, T. Elsaesser, E. T. J. Nibbering, and A. Rouzée, "Soft x-ray absorption spectroscopy of aqueous solutions using a table-top femtosecond soft x-ray source," J. Phys. Chem. Lett. **10**, 52–58 (2019).

29. T. Feng, A. Heilmann, M. Bock, L. Ehrentraut, T. Witting, H. Yu, H. Stiel, S. Eisebitt, and M. Schnörer, "27 W 2.1 μm OPCPA system for coherent soft x-ray generation operating at 10 kHz," Opt. Express **28**, 8724–8733 (2020).

30. I. Mantouvalou, K. Witte, D. Grötzsch, M. Neitzel, S. Günther, J. Baumann, R. Jung, H. Stiel, B. Kanngießer, and W. Sandner, "High average power, highly brilliant laser-produced plasma source for soft x-ray spectroscopy," Rev. Sci. Instrum. **86**, 035116 (2015).

31. P. Grünberg, R. Schreiber, Y. Pang, M. B. Brodsky, and H. Sowers, "Layered magnetic structures: evidence for antiferromagnetic coupling of fe layers across Cr interlayers," Phys. Rev. Lett. **57**, 2442–2445 (1986).

32. M. N. Baibich, J. M. Broto, A. Fert, F. N. Van Dau, F. Petroff, P. Etienne, G. Creuzet, A. Friederich, and J. Chazelas, "Giant magnetoresistance of (001)Fe/(001)Cr magnetic superlattices," Phys. Rev. Lett. **61**, 2472–2475 (1988).

33. G. Binasch, P. Grünberg, F. Saurenbach, and W. Zinn, "Enhanced magnetoresistance in layered magnetic structures with antiferromagnetic interlayer exchange," Phys. Rev. B **39**, 4828–4830 (1989).

34. D. Schick, S. Eckert, N. Pontius, R. Mitzner, A. Föhlisch, K. Holldack, and F. Sorgenfrei, "Versatile soft x-ray-optical cross-correlator for ultrafast applications," Struct. Dyn. **3**, 054304 (2016).

35. R. Jung, J. Tümmler, and I. Will, "Regenerative thin-disk amplifier for 300 mJ pulse energy," Opt. Express **24**, 883–887 (2016).

36. M. Brzhezinskaya, A. Firsov, K. Holldack, T. Kachel, R. Mitzner, N. Pontius, J. S. Schmidt, M. Sperling, C. Stamm, A. Föhlisch, and A. Erko,

"A novel monochromator for experiments with ultrashort x-ray pulses," J. Synchrotron Radiat. **20**, 522–530 (2013).

37. K. Holldack, J. Bahrdt, A. Balzer, U. Bovensiepen, M. Brzhezinskaya, A. Erko, A. Eschenlohr, R. Follath, A. Firsov, W. Frentrup, L. Le Guyader, T. Kachel, P. Kuske, R. Mitzner, R. Müller, N. Pontius, T. Quast, I. Radu, J.-S. Schmidt, C. Schöler-Langeheine, M. Sperling, C. Stamm, C. Trabant, and A. Föhlisch, "FemtoSpeX: a versatile optical pump-soft x-ray probe facility with 100 fs x-ray pulses of variable polarization," J. Synchrotron. Radiat. **21**, 1090–1104 (2014).

38. D. Schick, A. Bojahr, M. Herzog, C. von Korff Schmising, R. Shayduk, W. Leitenberger, P. Gaal, and M. Bargheer, "Normalization schemes for ultrafast x-ray diffraction using a table-top laser-driven plasma source," Rev. Sci. Instrum. **83**, 25104 (2012).

39. A. Koç, C. Hauf, M. Woerner, L. von Grafenstein, D. Ueberschaer, M. Bock, U. Griebner, and T. Elsaesser, "Compact high-flux hard x-ray source driven by femtosecond mid-infrared pulses at a 1 kHz repetition rate," Opt. Lett. **46**, 210–213 (2021).

40. F. Radu and H. Zabel, "Exchange bias effect of ferro-/antiferromagnetic heterostructures," in *Magnetic Heterostructures: Advances and Perspectives in Spinstructures and Spintransport*, Springer Tracts in Modern Physics, H. Zabel and S. D. Bader, eds. (Springer, 2008), pp. 97–184.

41. D. Schick, "udkm1dsim - a python toolbox for simulating 1D ultrafast dynamics in condensed matter," Comput. Phys. Commun. **266**, 108031 (2021).

42. M. Elzo, E. Jal, O. Bunau, S. Grenier, Y. Joly, A. Y. Ramos, H. C. N. Tolentino, J. M. Tonnerre, and N. Jaouen, "X-ray resonant magnetic reflectivity of stratified magnetic structures: Eigenwave formalism and application to a W/Fe/W trilayer," J. Magn. Reson. **324**, 105–112 (2012).

43. A. Jonas, K. Dammer, H. Stiel, B. Kanngiesser, R. Sánchez-de-Armas, and I. Mantouvalou, "Transient sub-nanosecond soft x-ray NEXAFS spectroscopy on organic thin films," Anal. Chem. **92**, 15611–15615 (2020).

44. M. Blume and D. Gibbs, "Polarization dependence of magnetic x-ray scattering," Phys. Rev. B **37**, 1779–1789 (1988).

45. J. K. Dewhurst, P. Elliott, S. Shallcross, E. K. Gross, and S. Sharma, "Laser-induced intersite spin transfer," Nano Lett. **18**, 1842–1848 (2018).

46. F. Willems, C. von Korff Schmising, C. Strüber, D. Schick, D. W. Engel, J. K. Dewhurst, P. Elliott, S. Sharma, and S. Eisebitt, "Optical inter-site spin transfer probed by energy and spin-resolved transient absorption spectroscopy," Nat. Commun. **11**, 871 (2020).

47. B. Koopmans, G. Malinowski, F. Dalla Longa, D. Steiauf, M. Fähnle, T. Roth, M. Cinchetti, and M. Aeschlimann, "Explaining the paradoxical diversity of ultrafast laser-induced demagnetization," Nat. Mater. **9**, 259–265 (2010).

48. D. Schick, M. Herzog, A. Bojahr, W. Leitenberger, A. Hertwig, R. Shayduk, and M. Bargheer, "Ultrafast lattice response of photoexcited thin films studied by x-ray diffraction," Struct. Dyn. **1**, 064501 (2014).

49. E. Jal, V. López-Flores, N. Pontius, T. Ferté, N. Bergeard, C. Boeglin, B. Vodungbo, J. Lüning, and N. Jaouen, "Structural dynamics during laser-induced ultrafast demagnetization," Phys. Rev. B **95**, 184422 (2017).

50. M. Kretschmar, J. Tuemmler, B. Schütte, A. Hoffmann, B. Senfftleben, M. Mero, M. Sauppe, D. Rupp, M. J. J. Vrakking, I. Will, and T. Nagy, "Thin-disk laser-pumped OPCPA system delivering 44 TW few-cycle pulses," Opt. Express **28**, 34574–34585 (2020).

51. A. S. Disa, M. Fechner, T. F. Nova, B. Liu, M. Först, D. Prabhakaran, P. G. Radaelli, and A. Cavalleri, "Polarizing an antiferromagnet by optical engineering of the crystal field," Nat. Phys. **16**, 937–941 (2020).

52. D. Afanasiev, J. R. Hortensius, B. A. Ivanov, A. Sasani, E. Bousquet, Y. M. Blanter, R. V. Mikhaylovskiy, A. V. Kimel, and A. D. Caviglia, "Ultrafast control of magnetic interactions via light-driven phonons," Nat. Mater. **20**, 607–611 (2021).